Capability of cross-hole electrical configurations for monitoring rapid plume migration experiments

F. Bellmunt[1*], A. Marcuello[1], J. Ledo[1] and P. Queralt[1]

[1] Geomodels - Departament de Geodinàmica i Geofísica. Barcelona Knowledge Campus (BKC). Universitat de Barcelona. Martí i Franquès s/n, 08028. Barcelona, Spain.

[*] Corresponding author e-mail: fbellmunt@ub.edu

ABSTRACT

Cross-hole electrical resistivity tomography is a useful tool in geotechnical, hydrogeological or fluid/gas plume migration studies. It allows to better characterizing deep subsurface structures and monitoring the involved processes. However, due to the large amount of possible four-electrode combinations between boreholes, the choice of the most efficient ones for rapid plume migration experiments (real-time monitoring) becomes a challenge. In this work, a numerical simulation to assess the capabilities and constraints of the most common cross-hole configurations for real-time monitoring is presented. Four-electrode configurations, sensitivity, dependence on the body location and amount of data were taken into account. The analysis of the anomaly detection and the symmetry on the sensitivity pattern of the cross-hole configurations allowed significantly reducing amount of data, in order to adjust acquisition time to the length of the dynamic process to be monitored, maintaining the maximum potential resolution of each configuration. The obtained results also highlighted the benefit of using configurations with complementary sensitivity pattern.

Keywords: cross-hole electrical resistivity tomography, resistivity imaging, dataset optimization.

1. INTRODUCTION

Cross-hole electrical resistivity tomography (CHERT) consists of acquiring electrical resistivity measurements between two or more boreholes and aims imaging the resistivity distribution between them. Since electrodes are down in boreholes, CHERT allows imaging deeper areas and helps to improve resolution at depth.

Monitoring time-lapse evolution of fluids or gas plumes injected in boreholes (Barker and Moore, 1998; Slater et al., 2000; Kiessling et al., 2010; Hagrey and Petersen, 2011; Carrigan et al., 2013) or urban tunnel drillings (Denis et al., 2002; Gibert et al., 2006; Chambers et al., 2007; Bellmunt et al., 2012) using CHERT is becoming common because of the simple and quick data acquisition. However, when rapid migration processes are going to be monitored, the acquisition time becomes critical because it has to be adjusted to the length of the dynamic process. Significant resistivity changes during data acquisition can lead to low resolution images and low convergence of data (Wilkinson et al., 2010). The acquisition time is directly related to the amount of data and the multichannel acquisition efficiency (Bellmunt and Marcuello, 2011). As a general rule, increasing the amount of data will increase resolution, but the improvement begins to level off at large amount of data. The dataset that includes all the standard and non-standard (non-reciprocal) measurements, named comprehensive dataset (Stummer et al., 2004), will contain the maximum resolution. However, the huge amount of data makes it of unrealistic application.

The recent researches in electrical resistivity tomography are focused on searching limited electrode combinations, comparable in quality to the comprehensive dataset, by developing optimization algorithms. In these algorithms, the cumulative sensitivity (Furman et al., 2004; Hennig and Weller, 2005) or the model resolution (Stummer et al., 2004; Wilkinson et al., 2006; Loke et al., 2014a) improvement is evaluated while groups of combinations of the comprehensive dataset are sequentially added to a small base one. Nyquist et al. (2007) compared the optimized array of Stummer et al. (2004) and the standard dipole-dipole array and they conclude that the first one provides better resolution mainly at depth. But they noticed that the optimized dataset required three times the standard dipole-dipole acquisition time. Wilkinson et al. (2012) constrained the optimization algorithms to choose what they call near-optimal configurations but well suited for multichannel acquisitions.

At present, the optimization algorithms are not included in the commercial software for resistivity data inversion. Therefore, most researchers still use the traditional CHERT configurations. The extended use of these configurations has allowed researchers to establish their main characteristics (Yang and Ward, 1985; Bing and Greenhalgh, 1997, 2000; Wilkinson et al., 2008). As a general rule in electrical resistivity tomography, the smaller the distance between the active electrodes of each borehole, the larger the influence on data of the immediately surrounding boreholes, and the larger this distance, the larger the influence on data of the central area of the panel between the involved boreholes. However, larger distances are more affected by lateral effects, heterogeneities located outside the panel between the involved boreholes, which can produce shadow effects in the resultant inversion models (Nimmer et al., 2008). Tsourlos et al. (2011) detected this shadow effects on single borehole-to-surface ERT experiments and concluded they were consequence of the high symmetric sensitivity pattern of the in-hole configurations (with all the electrodes in the same borehole). They proposed a modified inversion scheme based on a weighted factor, to avoid the shadow or symmetric effects of the in-hole configurations. But, they pointed out the difficulty of defining an objective threshold of asymmetry to use in an automatic way and of removing these artifacts completely.

These inversion artifacts could be removed using the model stacking technique proposed by Leontarakis and Apostolopoulos (2012), which consists on stacking different configurations inversion models to remove the particular artifacts from each configuration. They proved the efficiency of this technique from laboratory studies. However, the acquisition of various configurations could involve too much time for monitoring studies.

This work proposes an organized way to select the most adequate electrode combinations for rapid CHERT monitoring (acquisition protocol) in order to reduce: 1) the amount of data and acquisition time, but maintaining the maximum potential benefit of each configuration, and 2) the shadow effects inherent to configurations with highly symmetric sensitivity pattern. The abilities of the most common CHERT configurations are evaluated and compared, using 2D numerical models, to reduce the uncertain on the acquisition protocol using each configuration, or a mixed one.

2. DATA ANALYSIS PROCEDURE

Following, we present the proposed methodology to analyze the CHERT configurations ability to plume migration monitoring. Figure 1 can help to better understand the meaning of the next expressions, although it will be explained later. The procedure consists of three steps:

The first step consists in calculating the relative apparent resistivity variation produced using each configuration by considering the addition of a resistivity anomaly in a homogeneous half-space. This resistivity variation is related to the anomaly detection capability and it is calculated by the following expression:

$$AD = max\left|\frac{\rho_a - \rho_{HM}}{\rho_{HM}}\right| \qquad (1)$$

where AD: Anomaly Detection value (in absolute value); ρ_{HM}: resistivity value obtained using a homogeneous earth. ρ_a: apparent resistivity value obtained including a resistivity anomaly in the homogeneous earth. Both resistivity values are calculated using the same electrode combination. Similar expressions to evaluate the anomaly effect can be found in Militzer et al. (1979).

The second step consists in calculating the relative difference between two apparent resistivity values calculated for the same electrode combination but one value considering an anomaly located inside the panel between the two involved boreholes and the other one, with the same anomaly located outside the panel. The difference between the two responses is related to the symmetry on the sensitivity pattern. If no apparent resistivity differences between the two responses are detected, it will imply low capacity to resolve the plume migration direction (highly symmetrical sensitivity pattern). Therefore, the model interpretation could be uncertain. In this work, this difference is calculated by the following expression:

$$IOS = max\left|\frac{2(\rho_{a_{in}} - \rho_{a_{off}})}{\rho_{a_{in}} + \rho_{a_{off}}}\right| \qquad (2)$$

where IOS: In-panel/Off-panel Sensitivity value (absolute value); $\boldsymbol{\rho_{a_{in}}}$: apparent resistivity value obtained using a resistivity anomaly inside the panel between two involved boreholes; $\boldsymbol{\rho_{a_{off}}}$: apparent resistivity value obtained using the same resistivity anomaly as before but located outside the panel.

The third step consists in selecting the top rated four-electrode combinations of each configuration using the first and second steps results. As a general rule, the proposed criterion is to choose only the electrode combinations with the highest AD and IOS, which will lead to reduce the amount of data and the symmetric artifacts. However, to make a proper election, acquisition time, desired resolution and signal-to-noise ratio have to be considered.

3. APPLICATION

In order to evaluate the CHERT configurations ability to plume migration monitoring (steps 1 and 2 of the data analysis procedure), a 2D numerical experiment was designed. Following, we describe the resistivity model and the CHERT configurations used.

3.1. Dynamic resistivity model

The dynamic model presented here (Figure 1) was designed to get knowledge about the AD, and specially the IOS, of the CHERT configurations during different stages of a plume migration process. It consists of three in-line boreholes, 10 m apart and 20 m in depth, located in a 100 ohm·m homogeneous half-space. 21 electrodes (1 m-spaced) were placed into each borehole. The plume was simulated using three square bodies of side length twice the electrode distance and centered at three different positions of constant depth: 1, 3 and 5 m from BH2, named stages A, B and C, respectively.

Two resistivity contrasts (Rc=ρplume/ρhalf space), emulating a saline (Rc=0.1) and a gas (Rc=10) plumes, were considered.

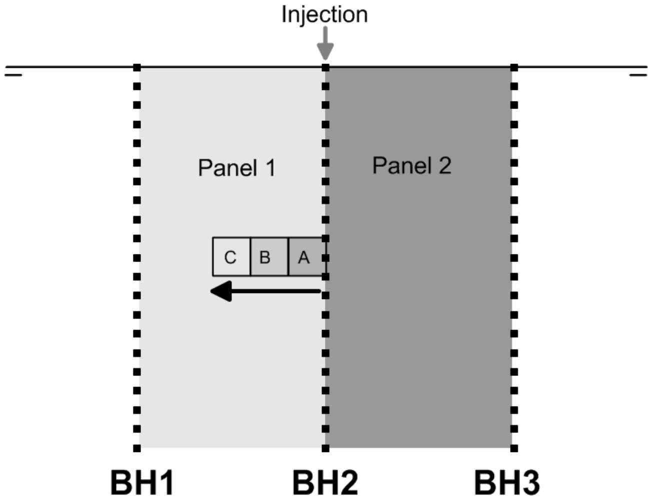

Figure 1. Dynamic model and stages used to simulate different positions of a plume in a migration process. Small vertical black squares represent the electrode location into boreholes BH1, BH2 and BH3; black arrow and grey squares (named A, B and C) simulate the plume direction and position at stages A, B and C, respectively. Panel 1 (light grey colored) represents the cross-hole measurements acquired between BH1 and BH2, and panel 2 (dark grey colored), the cross-hole measurements acquired between BH2 and BH3.

The two panels between the three involved boreholes in Figure 1 have been grey colored to differentiate between the cross-hole measurements acquired using BH1-BH2 electrodes (Panel 1) and the ones acquired using BH2-BH3 electrodes (Panel 2). The AD (step 1) was evaluated comparing two panel 1 responses, one with and one without the imbedded anomaly (plume), for each model stage. The IOS (step 2) was evaluated comparing panel 1 and panel 2 responses for each model stage. Comparisons were always carried out using the same electrode combination. Note that using the two panels in step 2, two opposite directions for the plume migration were considered: inward the panel 1 (if boreholes BH1 and BH2 are used) and outward the panel 2 (if boreholes BH2 and BH3 are used). As commented before, configurations with no differences between panel 1 and panel 2 responses at each stage can lead to obtain resistivity images of uncertain interpretation.

3.2. CHERT configurations

In this work, we use the term "dipole", instead of “bipole”, to designate the CHERT configurations because of their extensive use in the surface configurations notation, but we add the prefix CH (cross-hole). This experiment was focused on the CH dipole-dipole (CH AM-BN and CH AB-MN) and the CH pole-tripole (CH AMN-B/A-BMN) arrays (Bing and Greenhalgh, 2000; Goes and Meekes, 2004). Capital letters designate the electrodes (A and B represent the current electrodes and, M and N, the potential ones) and their position into the boreholes (i.e. AM-BN means that the A and M electrodes are located in one borehole and the B and N, in the other one). Geometry and sensitivity patterns of the configurations used are summarized in Figure 2 and Figure 3, respectively.

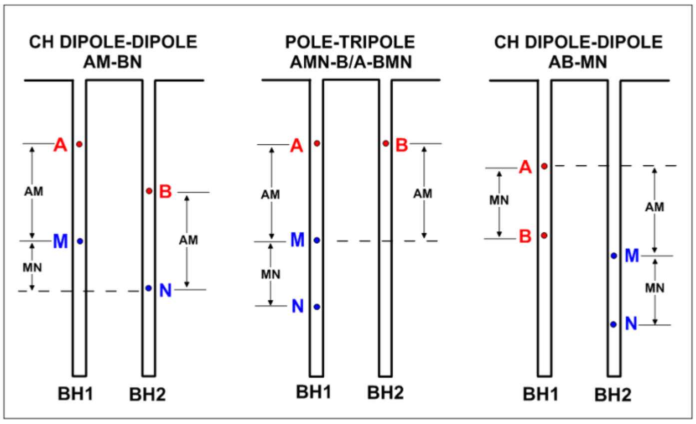

Figure 2. Electrode distribution schemes for the CH dipole-dipole arrays (CH AM-BN and CH AB-MN) and the CH pole-tripole array with the MN dipole in the two boreholes (CH AMN-B/A-BMN). Capital letters and red/blue points designate the electrode name and their position into the boreholes (A and B represent the current electrodes and, M and N, the potential ones); AM: vertical distance between the current and the potential electrodes; MN: vertical distance between the potential electrodes.

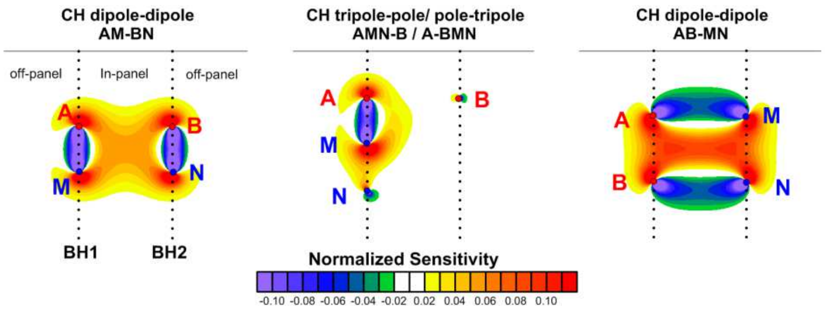

Figure 3. Sensitivity patterns for the CH dipole-dipole (CH AM-BN and CH AB-MN) and the CH pole-tripole (CH AMN-B). The letters A and B represent the current electrodes and, M and N, the potential ones. In each configuration, sensitivity was normalized by its maximum value.

The configurations responses to the model presented in Figure 1 (stages A to C) were calculated using the commercial Earthimager 2D software (AGI, Advanced Geosciences, Inc.) with a lateral extended four-element mesh. The CH dipole-dipole AM-BN responses were calculated moving up and down the electrodes but maintaining the distance between the electrodes A and M always equal to the B and N electrodes distance, which resulted in a datasets of 5740 combinations, 2870 per panel (see Figure 1). The CH dipole-dipole AB-MN responses were calculated using all the possible distances between the electrodes but using the current electrodes (A and B) distance always equal to the potential electrodes (M and N) one, resulting in 5740 combinations (2870 per panel). The CH pole-tripole (AMN-B/A-BMN) responses were calculated using all the possible distances between the current and potential dipoles but maintaining the electrodes A and B at the same depth and using five MN distances, which resulted in 3080 combinations (1540 per panel). As can be seen, the AM and MN distances used do not include all the possible four-electrode combinations for each configuration, however they are considered the most representative combinations for each configuration.

4. RESULTS

Following, we present the results obtained by applying the proposed methodology to the CH dipole-dipole (AM-BN, AB-MN) and the CH pole-tripole arrays using the dynamic model presented in Figure 1 and considering two resistivity contrasts, *Rc*=0.1 and *Rc*=10. The magnitudes of AD and IOS for each configuration were calculated versus different AM and MN distances (Figure 2).

4.1. Resistivity contrast *Rc*=0.1

The results of applying the presented methodology to three plume bodies of resistivity 10 ohm·m in a 100 ohm·m half-space are presented below.

4.1.1. Anomaly detection value, AD

Figure 4 shows the AD results for each configuration versus different AM and MN distances. The maximum AD is obtained for the CH dipole-dipole AB-MN and CH pole-tripole arrays at all the three stages of the dynamic model.

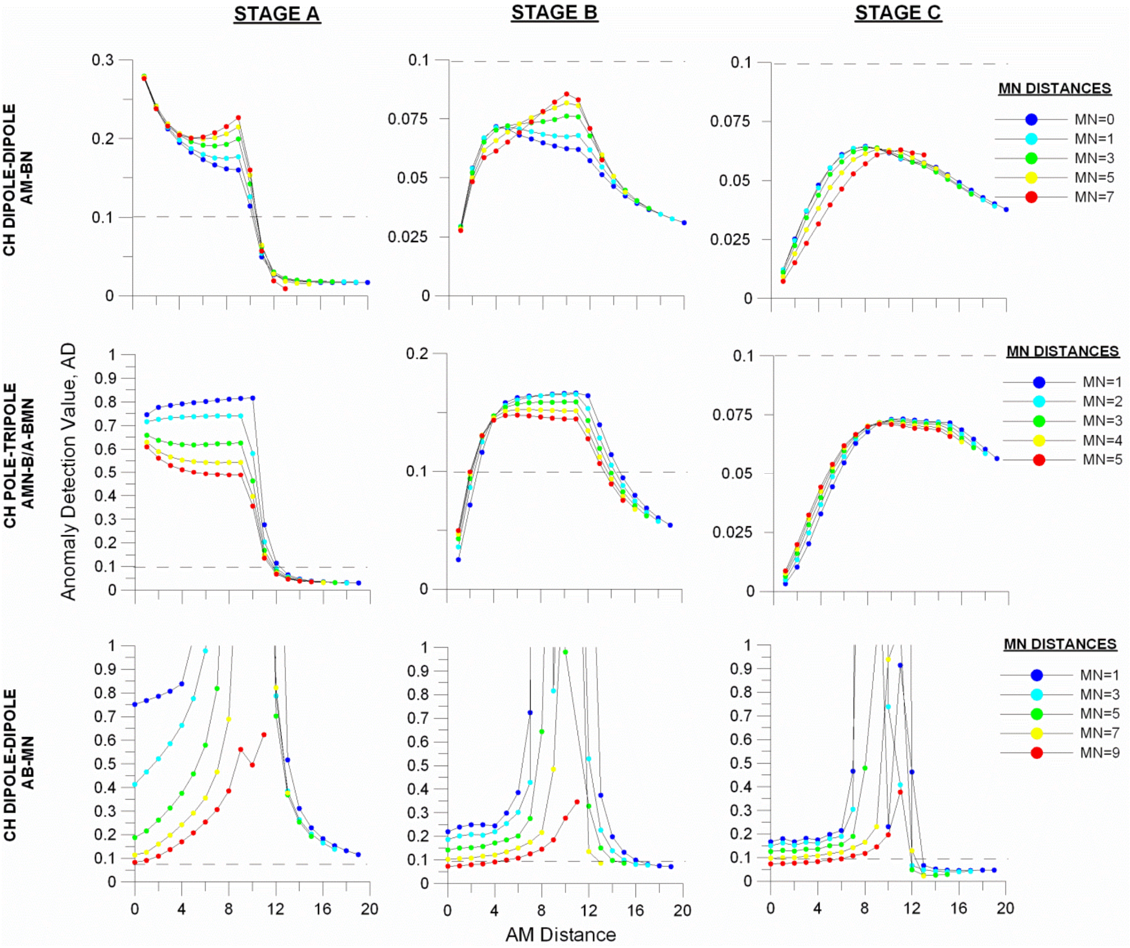

Figure 4. Anomaly detection value (AD) calculated for the CH dipole-dipole (AM-BN and AB-MN) and the CH pole-tripole arrays at the three stages (A, B and C) of the dynamic model using a resistivity contrast *Rc*=0.1. Maximum absolute relative resistivity variation (Y-axis) versus AM (X-axis) and MN (colored lines) distances. Dashed line indicates a 10% of resistivity change as guidance only.

The AD presents a quite similar behavior for all the three configurations used (Figure 4). As expected, the higher AD is obtained at stage A (Figure 1), because of the plume is closer to the boreholes. When the plume moves from stage A to stage C, the AD decreases and larger AM distances are needed to detect the plume. Once the maximum value is reached, the AD decreases and tends to level off. This decrease is rapidly accentuated when the AM distance becomes higher than the boreholes distance. However, each configuration presents a slightly different AD pattern (Figure 4):

For the CH AM-BN array, the maximums AD obtained (equation 1) at stages A, B and C are 28%, 8% and 6%, respectively. In this case, a secondary AD peak is exhibit for AM distances similar to the boreholes distance (10 m) as the MN distance increases. This secondary peak becomes higher than the primary one at the stage B of the dynamic model.

For the CH pole-tripole array (AMN-B/A-BMN), the maximums AD obtained at stages A, B and C are 82%, 17% and 7%, respectively. Once the maximum values are reached, this configuration presents a flat area of maximum AD before starting to decrease. The AD decreases as the MN distance increases.

The CH AB-MN array exhibits extremely high values (higher than 100%) for all the three model stages for AM values similar to the boreholes distance. For AM distances lower than six, out of the interval of extremely high values, maximums AD at stages A, B and C are of about 80%, 25% and 20%, respectively. As the MN distance increases, the AD decreases.

4.1.2. In-panel/off-panel sensitivity value, IOS

Figure 5 shows the IOS results for each configuration versus different AM and MN distances. The maximum IOS using Rc=0.1 is obtained for the CH dipole-dipole AB-MN and the CH pole-tripole arrays at all the stages of the dynamic model.

The IOS and the AD present a similar behavior: the highest values are obtained at stage A, and as the plume moves from stage A to C, the IOS decreases. Once the maximum IOS is reached, it rapidly decreases. However, the maximum IOS is always obtained using AM=10-12 for all the studied configurations and stages of the model.

For the CH AM-BN array, the maximums IOS obtained at the stages A, B and C are 20%, 8% and 6%, respectively. As the MN values increase, the IOS increases.

For the CH pole-tripole array, the maximum IOS obtained at the stages A, B and C are 70%, 10% and 9%, respectively. In this case, as the MN values increase, the IOS decreases.

The CH AB-MN array presents the highest IOS, but extremely high values are detected for AM distances similar to the boreholes distance. As the MN values increase, the IOS decreases.

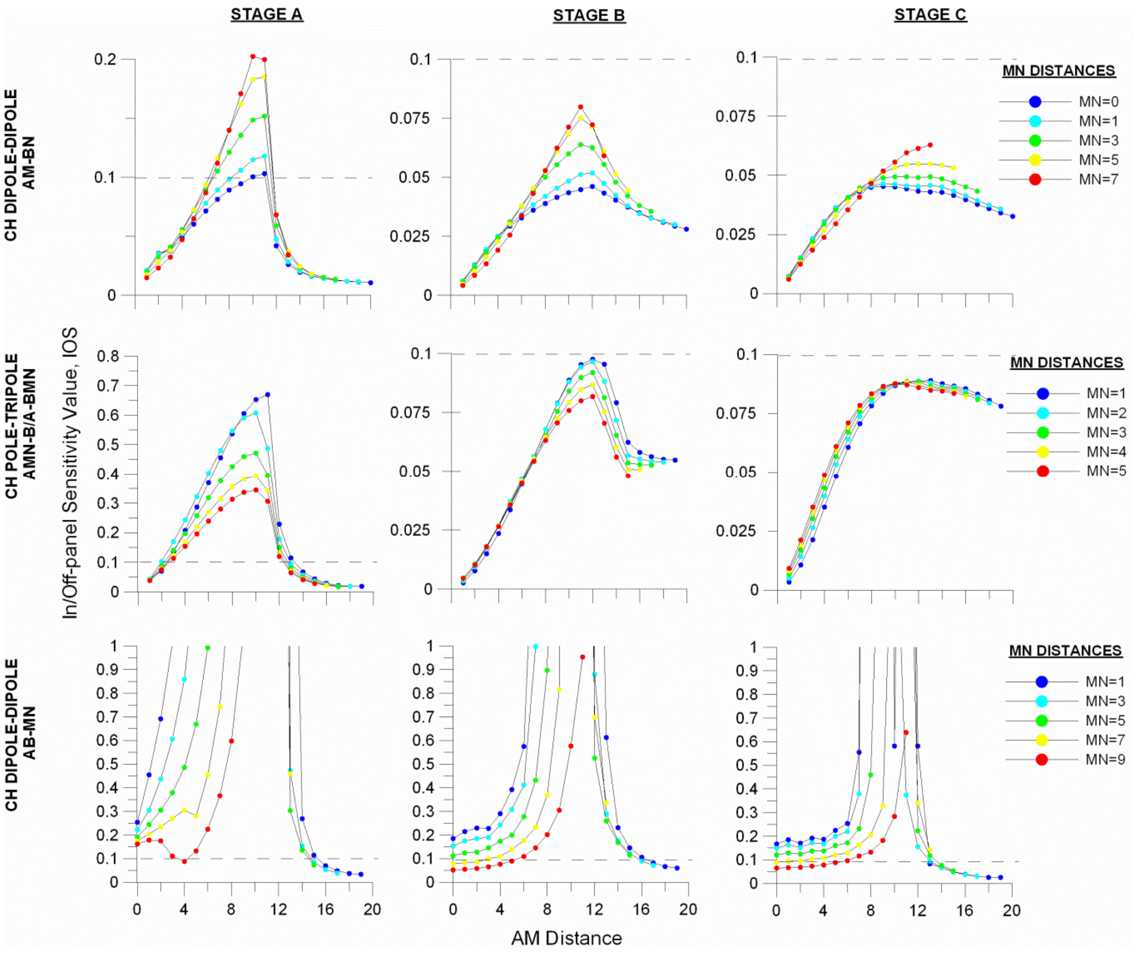

Figure 5. In-panel/off-panel sensitivity value (IOS) calculated using the CH dipole-dipole (AM-BN and AB-MN) and the CH pole-tripole arrays for all the three stages (A, B and C) of the dynamic model and a resistivity contrast, *Rc*=0.1. Maximum absolute relative apparent resistivity difference (Y-axis) versus AM (X-axis) and MN (colored lines) distances. Dashed line indicates a 10% of resistivity difference as guidance only.

4.2. Resistivity contrast *Rc*=10

The procedure application results, obtained using plume bodies of 1000 ohm·m in a 100 ohm m half-space, are presented below.

4.2.1. Anomaly detection value, AD

Figure 6 shows the main results obtained for the AD using *Rc*=10. The curves obtained using *Rc*=0.1 and *Rc*=10 (Figure 4 and 6) show that the AD follows a similar behavior in front of different resistivity contrasts but with slightly different values. In general, the AD obtained using *Rc*=10 is slightly lower than the one reached using *Rc*=0.1. Therefore, the results obtained using *Rc*=10 will be explained mainly focused on the differences observed from the previous resistivity contrast.

For the CH AM-BN array, the maximums AD obtained at stages A, B and C are 16%, 9% and 8%, respectively. In this case, as the MN distances increase, the secondary AD peak becomes higher than the primary one at all the stages of the dynamic model.

For the CH pole-tripole array, the maximum AD obtained at stages A, B and C are 82%, 14% and 7%, respectively. In this case, the maximum AD tends to level off but much slowly than it does using *Rc*=0.1 (compare Figure 4 and 6).

The CH AB-MN array exhibits the same extremely high values as the ones obtained using *Rc*=0.1. However, for small AM distances, the AD increases faster than using a conductive anomaly (compare Figure 4 and 6).

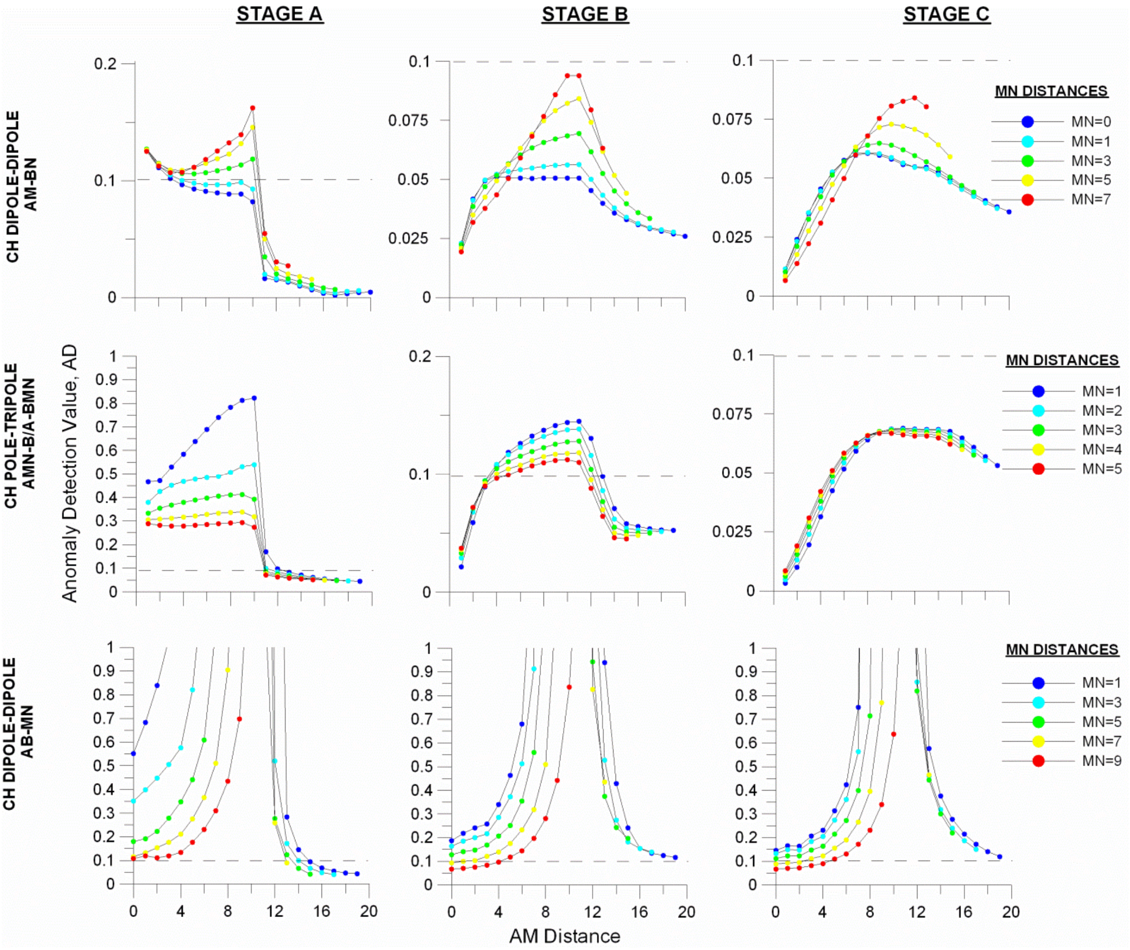

Figure 6. Anomaly detection value (AD) calculated for the CH dipole-dipole (AM-BN and AB-MN) and the CH pole-tripole arrays at the three stages (A, B and C) of the dynamic model using a resistivity contrast, *Rc*=10. Maximum absolute relative apparent resistivity variation (Y-axis) versus AM (X-axis) and MN (colored lines) distances using panel 1. Dashed line indicates a 10% of resistivity change as guidance only.

4.2.2. In-panel/off-panel sensitivity value, IOS

Figure 7 shows the main results for the IOS using *Rc*=10. As the AD does, the IOS follows a similar behavior for different resistivity contrasts. Therefore, the results obtained using *Rc*=10 will be explained based on the differences observed from the previous resistivity contrast results.

For the CH AM-BN array, the maximums IOS obtained at the stages A, B and C are 27%, 11% and 9%, respectively, which are slightly higher than the ones reached using *Rc*=0.1 (compare Figure 5 and Figure 7). As the MN value increases, the maximum IOS increases.

For the CH pole-tripole array, the maximum IOS obtained at the stages A, B and C are 56%, 12% and 7%, respectively. In this case, the values obtained using *Rc*=10 are only higher than the ones reached using *Rc*=0.1 at the stage B of the dynamic model (compare Figure 5 and Figure 7). As the MN value increases, the IOS decreases.

The CH AB-MN array presents the highest IOS, but extremely high values at AM distances similar to the boreholes distance. As the MN value increases, the IOS decreases.

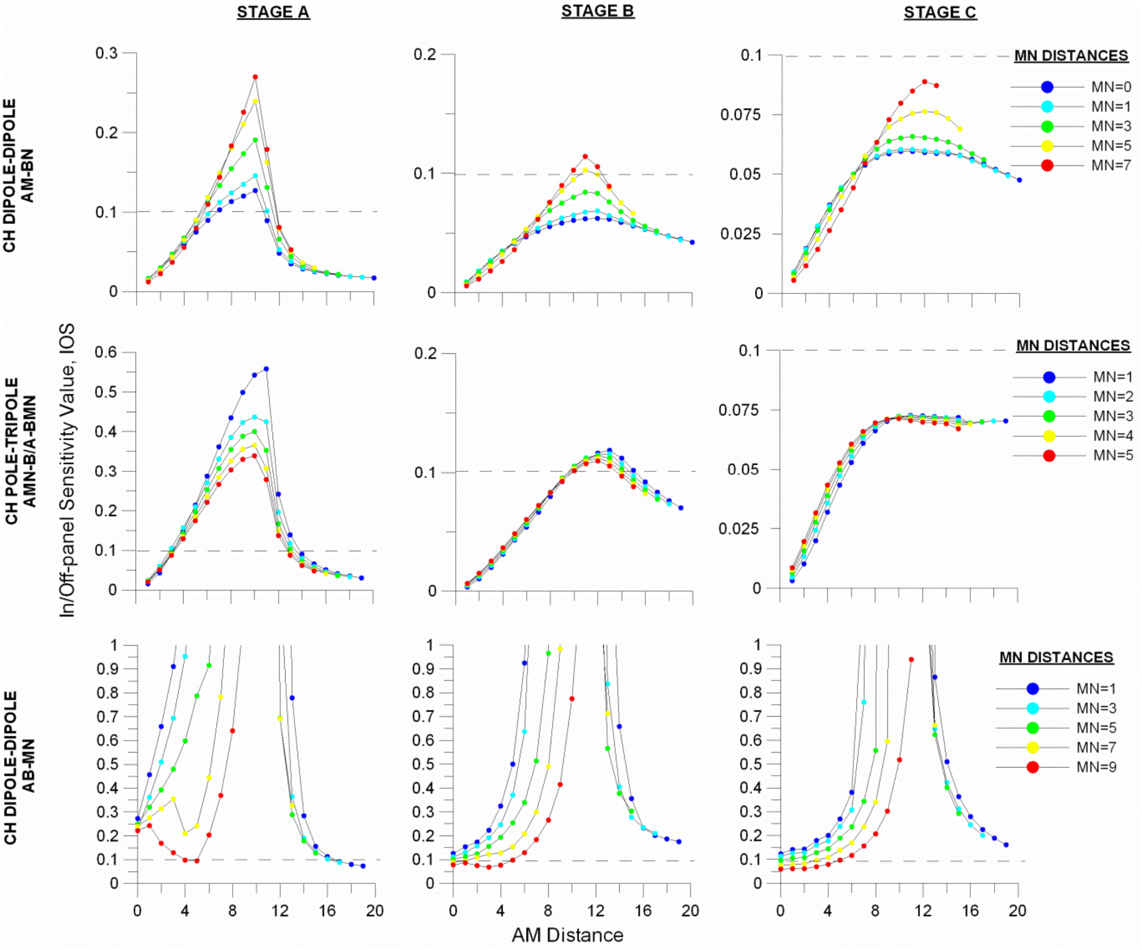

Figure 7. In-panel/off-panel sensitivity value (IOS) calculated using the CH dipole-dipole (AM-BN and AB-MN) and the CH pole-tripole arrays for all the three stages (A, B and C) of the dynamic model and a resistivity contrast, *Rc*=10. Maximum relative apparent resistivity variation (Y-axis) versus AM (X-axis) and MN (colored lines) distances using panel 1 and panel 2 responses. Dashed line indicates a 10% of resistivity difference as guidance only.

4.3 Organized selection of the combinations

Once the configurations with the best capabilities have been detected, the selection of the most suitable combinations can be made in an organized way from the analysis data results. Taking into account the similar AD and IOS behavior observed using each configuration for different resistivity contrasts (Figures 4 to 7), the organized selection of the combinations is carried out in the same way regardless of the resistivity contrast to be resolved. The analysis results present the CH dipole-dipole AB-MN and the CH pole-tripole arrays as the best choices to migration monitoring using CHERT. In order to reduce amount of data for rapid migration monitoring, where the acquisition time is a critical aspect, the CH dipole-dipole AM-BN array, which shows the lowest AD and IOS, will not be taken into account.

Figures 4 to 7 show that the AD and the IOS patterns are repeated using different MN distances for each configuration. Therefore, the amount of data can be reduced by choosing only one MN distance per configuration. As a general rule, the electrode combinations that correspond to MN values with the highest AD and IOS will offer the maximum potential resolution for monitoring. The number of AM distances has to be chosen in order to cover the central region of the panel (stage C) and to obtain the maximum benefit of the IOS.

Configurations with different (or complementary) sensitivity patterns contribute differently to the model resolution (Bing and Greenhalgh, 1997). Therefore, a mixed organized dataset will be the best choice. The final organized dataset was made by combining the CH pole-tripole array, taking only the combinations with MN=1 and AM=1-14 (350 combinations per panel), and the CH dipole-dipole AB-MN one with MN=3 and AM=0±5 (168 data per panel). The reason for this choice, using the CH dipole-dipole AB-MN array, will be treated in the discussion section. This mixed organized dataset resulted in 518 combinations per panel (Figure 1).

5. DATA INVERSION

We carried out the inversion of the mixed organized dataset using the dynamic model presented in Figure 1 and two resistivity contrasts, Rc=0.1 and Rc=10. In order to establish the maximum potential model resolution that can be achieved using the top rated configurations, we made the inversion of the CH pole-tripole dataset with 1540 data per panel and the CH dipole-dipole AB-MN one with 1750 data per panel, either individually or in a mixed one (3290 data per panel). The CH AM-BN inversion models are also presented for comparison. The inversion models are presented in Figure 8 (Rc=0.1) and Figure 9 (Rc=10). Each inversion model included panel 1 and panel 2 responses.

The inversion of the datasets was carried out using the commercial Res2dinvx64 software (Geotomo software) with the robust inversion method. To simulate the effect of experimental errors, we added noise using the following expression (Bellmunt and Marcuello, 2011):

$$\Delta R= R\delta + \chi$$

where R is the error-free model response, and δ and χ are random numbers. δ follows a normal distribution with zero mean and standard deviation σ, and χ a uniform distribution in the interval [-ε, +ε]. These two random numbers (δ, χ) simulate the relative accuracy (δ) and the instrumental resolution (χ). A values of 0.015 for σ and 10^{-4} V/A for ε were considered.

As can be seen in Figure 8 (Rc=0.1), the CH dipole-dipole (AM-BN and AB-MN) and the CH pole-tripole inversion models are not able to fully resolve the dynamic experiment presented here. Although the plume body is located inside the panel 1, the CH AM-BN and the CH pole-tripole inversion models show an artifact on panel 2 in a “symmetric” location (Nimmer et al., 2008; Tsourlos et al., 2011). The CH AB-MN inversion models present much more artifacts than the previous ones, but they are mainly distributed along boreholes. The inversion models obtained joining them in a mixed dataset reach the maximum resolution and are able to recover all the stages of the dynamic model. The inversion models obtained using the organized dataset are able to track the plume as well as the complete mixed one.

The inversion models obtained using a resistivity contrast, *Rc*=10, show less artifacts than the obtained using *Rc*=0.1, but the plume resistivity value is worst recovered (Figure 9). In this case, individual and mixed inversions using the CH pole-tripole and the CH dipole-dipole AB-MN datasets are able to resolve the dynamic model, but the maximum resolution is achieved using the mixed one. The organized dataset is able to resolve all the stages of the dynamic model, but the anomaly resistivity value at the stage C is worst recovered than using the complete mixed one.

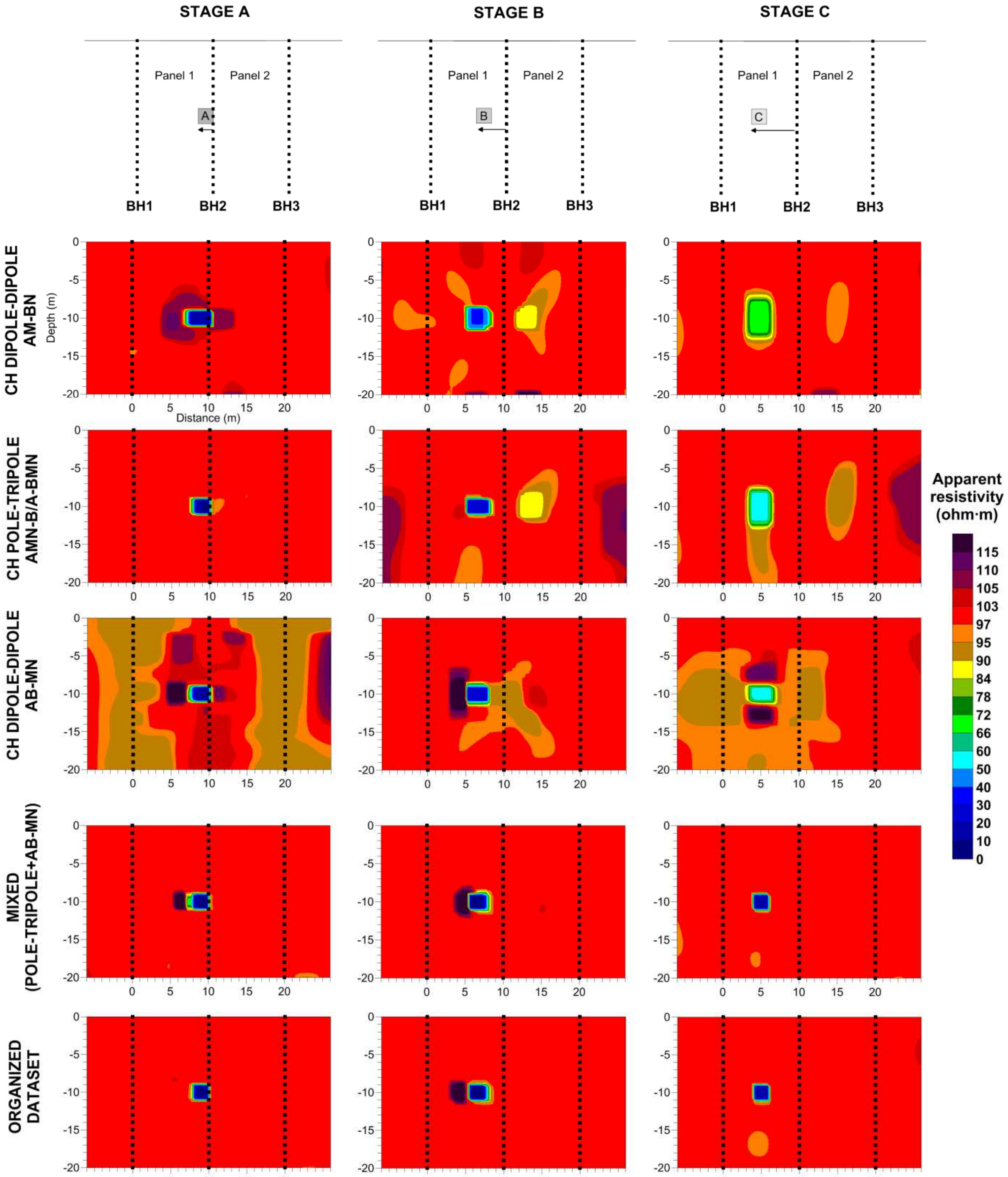

Figure 8. Inversion models obtained using (from top to bottom): the CH dipole-dipole AM-BN (5740 data), the CH pole-tripole (3080 data), the CH dipole-dipole AB-MN (3500 data), the complete mixed (CH pole-tripole and CH dipole-dipole AB-MN with 6580 data) and the organized (1036 data) datasets at the three stages (A, B and C) of the dynamic model. Resistivity contrast *Rc*=0.1. Root mean square (rms) =1.2%. Small vertical black squares represent the electrode location into boreholes (BH1, BH2 and BH3). Each inversion included panel 1 and panel 2 responses.

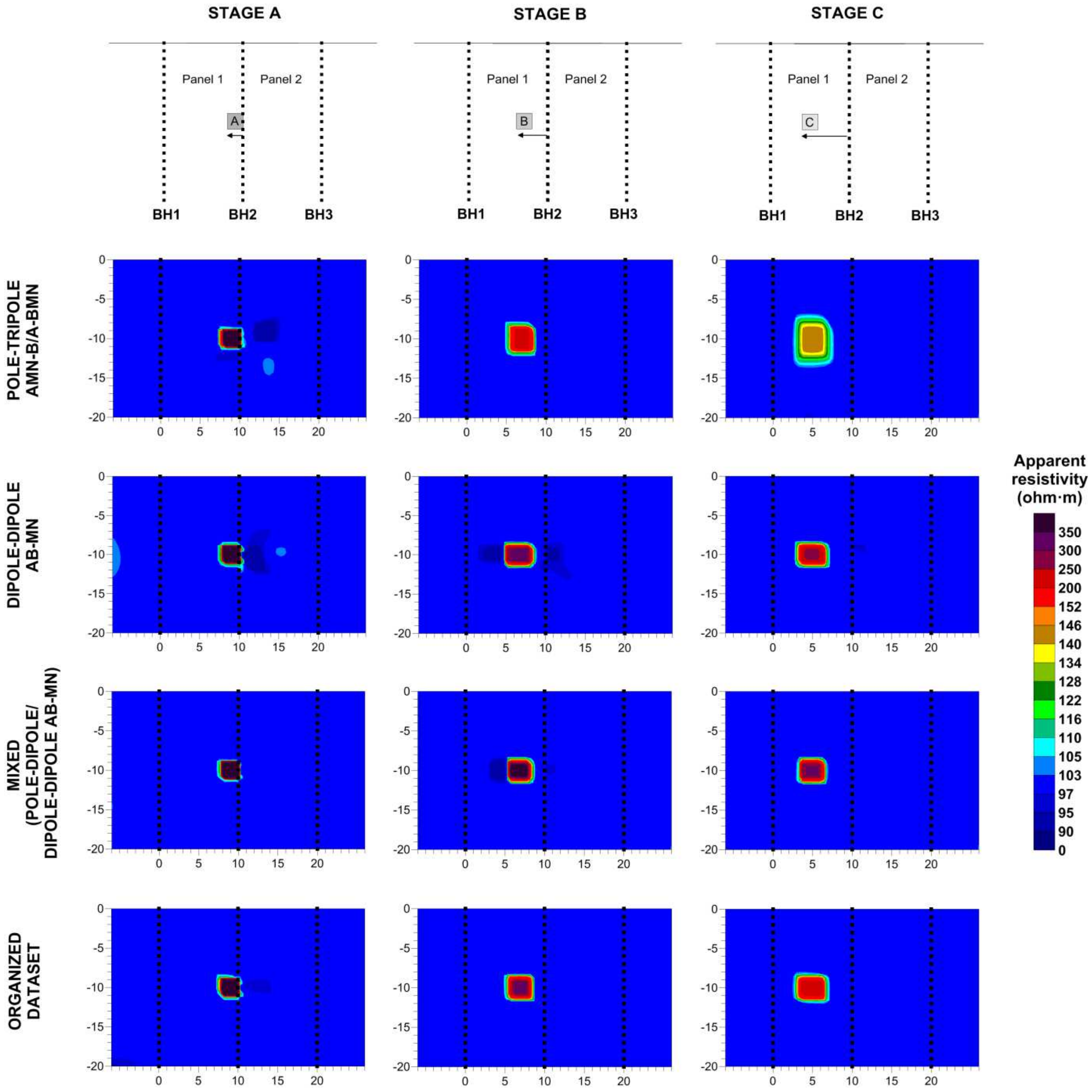

Figure 9. Inversion models obtained using (from top to bottom): the CH dipole-dipole AM-BN (5740 data), the CH pole-tripole (3080 data), the CH dipole-dipole AB-MN (3500 data), the complete mixed (CH pole-tripole and CH dipole-dipole AB-MN with 6580 data) and the organized (1036 data) datasets at the three stages (A, B and C) of the dynamic model using a resistivity contrast *Rc*=10. Root mean square (rms)=1.2%. Small vertical black squares represent the electrode location into boreholes (BH1 and BH2). Each inversion included panel 1 and panel 2 responses.

6. DISCUSSION

In this section we will discuss firstly the behavior observed for the AD using the CH dipole-dipole arrays and secondly the symmetric artifacts that affects the inversion models using *Rc*=0.1.

The AD graphs in Figures 4 and 7 show that the CH AM-BN array exhibits a secondary AD peak and the CH AB-MN array shows extremely high AD for all the three model stages. These maximums are related to an electric potential drop for those AM and MN distances. Usually, the geometric factor is used as a representative of the inverse of the electric potential for a homogeneous half-space (using a 1 ohm·m resistivity and an intensity of 1 A). High geometric factor values represent low potential readings, and inversely.

The Figure 10 shows the general behavior of the geometric factor for the CH dipole-dipole arrays. As can be seen in Figure 10A, as the MN distance increases, the geometric factor value for the CH AM-BN array becomes more upright at lower AM distances, and finally there is a sign change. The Figure 10B shows that the CH AB-MN geometric factor values rise highly when the AM distance increases. But in this case, the lower the MN distances, the higher the geometric factor values (or the lower the potential difference). In both cases, the rapid geometric factor increase means that there is a sharply drop in the electric potential at those AM and MN distances. In such a situation, measurements become highly sensitive, i.e. low resistivity variations, due to errors in the model responses calculation or in the measured data, can be in high resistivity changes. This explains why as the MN distance increases, the secondary AD peak becomes higher in the CH AM-BN array, and the existence of extremely high AD and IOS values in the CH AB-MN array.

Therefore, in order to maintain a trade-off between the AD and the electric potential level using the CH AB-MN array in the final organized dataset, the CH AB-MN measurements with MN=1-2 and AM>±5 were avoided. Note that the AM distance can be positive or negative using the CH AB-MN array (Figure 2).

Wilkinson et al. (2008) observed that the higher variations in apparent resistivity due to inaccurate electrode location (geometric factor errors) were obtained in such potential drop situations, and they developed the concept of geometric sensitivity to remove this unstable data. From the apparent resistivity expression ($\rho_a = kR$) we extend this unstable behavior, or error amplification, in potential drop situations to measured data. Therefore, to prevent undesired errors due to inaccurate electrode location (k) and data (R) errors, the AM and MN distances where the geometric factor increases, or decreases, in a sharply way would be avoided.

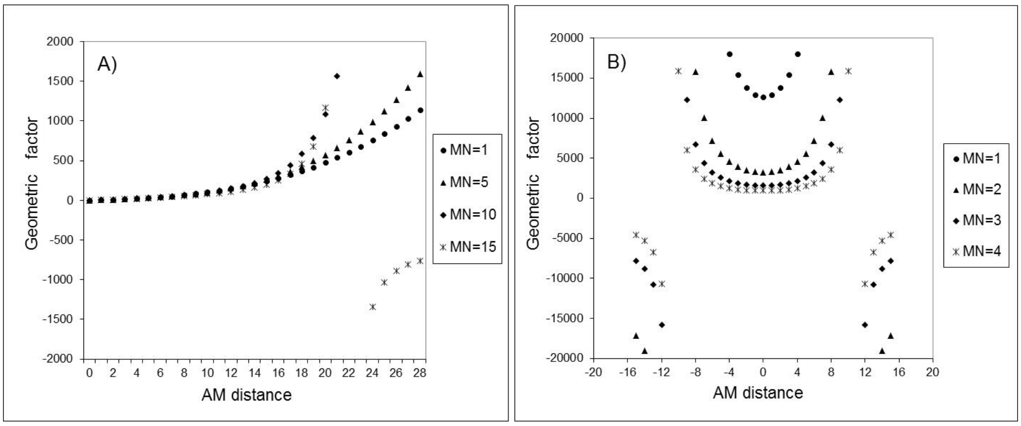

Figure 10. Geometric factor behavior obtained using the CH dipole-dipole arrays: A) CH AM-BN and B) CH AB-MN, with different AM and MN distances.

The CH AM-BN and CH pole-tripole inversion models show “symmetric” artifacts, using *Rc*=0.1, at the stages B and C of the dynamic model (Figure 8). The symmetric artifacts are related to the high symmetry on the sensitivity pattern (Tsourlos et al., 2011) along with to an insufficient angular coverage. The CH pole-tripole and the CH AM-BN arrays show IOS<10%, which means they have highly symmetric sensitivity patterns. The higher the symmetry on the sensitivity pattern, the higher the uncertain on the migration interpretation, and higher angular coverage needed to resolve the true anomaly location. Increasing amount of data by adding extra angular measurements (combinations with different AM or MN distances in each borehole) makes the artifact slightly lower, but they do not remove it at all, either using individual or mixed datasets.

The inversion results highlight the benefit of using the CH AB-MN to resolve the dynamic model presented here. Loke et al. (2014a) observed that the resolution of their optimized configurations decreased if the configurations with both current (or both potential) electrodes in the same borehole were excluded. As can be seen in this work, and in Loke et al. (2014b), the singularity acquisition problems using this configuration can be removed.

7. CONCLUSIONS

The analysis of the AD and IOS allows finding a trade-off between the required resolution and the available acquisition time (amount of data) for real-time monitoring. Understanding how each configuration works becomes a key aspect to be successful in monitoring short and quick dynamic processes, where the amount of data needs to be greatly reduced to adequate to the experiment length. The AD and IOS analysis has been applied to a specific dynamic model (using specific body lengths, resistivity contrasts and aspect ratio) and configurations, but it can be applied to different resistivity models and electrode combinations in a straightforward way.

The results highlight the benefit of joining various configurations because of their different sensitivity patterns: a lower angular coverage and a lower amount of data are needed to resolve a migration experiment. Considering most of the CHERT configurations have a quite similar sensitivity pattern, the CH AB-MN becomes necessary to resolve the dynamic model presented here and to remove the symmetric artifacts. As can be seen in this work, the singularity acquisition problems can be avoided to use this configuration in monitoring.

The similar IOS patterns observed for all the three configurations highlight the need for using AM lengths similar to the boreholes distance in cross-hole monitoring experiments.

The addition of more than one MN distance in the same dataset helps to improve resolution. However, before increasing amount of data by adding various MN distances, consider joining configurations with complementary sensitivity patterns. This provides better spatial resolution without greatly increasing the amount of data. In this work, a mixed organized dataset, which can be acquired in less than 10 minutes (1036 data) in a ten-simultaneous channels resistivity-meter, has been able to resolve the dynamic model presented here without the presence of symmetric artifacts. This allows acquiring multi-panel or 3D data in a time-effective way.

ACKNOWLEDGEMENTS

This work was partially supported by the Spanish Ministry of Economy and Competitiveness and EU FEDER funds under projects Geothercan (IPT-2011-1186-920000) and COMOSALTS (CGL2014-54118-C02-01-R) and by the Catalan Agency AGAUR through the Group "Geodynamics and Basin Analysis" (2014SGR467). We also thank the anonymous reviewers for their insightful comments and suggestions, which helped us to improve the manuscript.

REFERENCES

Barker, R., Moore, J., 1998. The application of time-lapse electrical tomography in groundwater studies. Lead. Edge 17, p. 1454-1458.

Bellmunt, F. and Marcuello, A., 2011. Method to obtain standard pseudosections from pseudo pole–dipole arrays. Journal of Applied Geophysics 75, p. 419–430.

Bellmunt, F., Marcuello, A., Ledo, J., Queralt, P., Falgàs, E., Benjumea, B., Velasco, V., Vázquez-Suñé, E., 2012. Time-lapse cross-hole electrical resistivity tomography monitoring effects of an urban tunnel. Journal of Applied Geophysics, 87, p. 60–70.

Bing, Z., Greenhalgh, S.A., 1997. A synthetic study on cross-hole resistivity imaging with different electrode arrays. Explor. Geophys. 28, p. 1-5.

Bing, Z., Greenhalgh, S.A., 2000. Cross-hole resistivity tomography using different electrode configurations. Geophysical Prospecting 48, p. 887–912.

Carrigan, C.R., Yang, X., LaBrecque, D.J., Larsen, D., Freeman, D., Ramírez, A.L., Daily, W., Newmark, R., Friedman, J., Hovorka, S., 2013. Electrical resistance tomographic monitoring of CO2 movement in deep geologic reservoirs. International Journal of Greenhouse Gas Control. 8, p. 401-408.

Chambers, J.E., Wilkinson, P.B., Weller, A.L., Meldrum, P.I., Ogilvy, R.D., Caunt, S., 2007. Mineshaft imaging using surface and crosshole 3D electrical resistivity tomography: A case history from the East Pennine Coalfield, UK. Journal of Applied Geophys. 62, p. 324-337.

Denis, A., Marache, A., Obellianne, T., Breysse, D., 2002. Electrical resistivity borehole measurements: an application to an urban tunnel site. J. Appl. Geophys. 50, p. 319-331.

Furman, A., Ferré, T.P.A., Warrick. A.W., 2004. Optimization of ERT surveys for monitoring transient hydrological events using perturbation sensitivity and genetic algorithms. Vadose Zone Journal 3, p. 1230-1239.

Gibert, D., Nicollin, F., Kergosien, B., Bossart, P., Nussbaum, C., Grislin-Mouëzy, A., Conil, F., Hoteit, N., 2006. Electrical tomography monitoring of the excavation damaged zone of the Gallery 04 in the Mont Terri rock laboratory: Field experiments, modelling, and relationship with structural geology. Appl. Clay Sci. 33, 21-34.

Goes, B.J.M. and Meekes, J.A.C., 2004. An effective electrode configuration for the detection of DNAPLs with electrical resistivity tomography. Journal of Environmental and Engineering Geophysics, 9, p. 127-141.

Hagrey, S.A. and Petersen, T., 2011. Numerical and experimental mapping of small root zones using optimized surface and borehole resistivity tomography. Geophysics, vol. 76, n 2, p. G25-G35.

Hennig, T. and Weller, A., 2005. Two dimensional object orientated focussing of geoelectrical multielectrode measurements. Proceedings of the 11th meeting of the EAGE Near Surface Geophysics Conference, Palermo, Italy.

Kiessling, D., Schmidt-Hattenberger, C., Schuett, H., Schilling, F., Krueger, K., Schoebel, B., Danckwardt, E., Kummerow, J., and the CO2sink Group, 2010. Geoelectrical methods for monitoring geological CO2 storage: First results from cross-hole and surface-downhole measurements from the CO2SINK test site at Ketzin (Germany). International Journal of Greenhouse Gas Control, 4, p. 816-826.

Leontakaris, K. and Apostolopoulos, G., 2012. Laboratory study of the cross-hole resistivity tomography: The Model Stacking (MOST) Technique. Journal of applied Geophysics, 80, p. 67-82.

Loke, M.H., Wilkinson, P.B., Chambers, J.E. and Strutt, M., 2014a. Optimized arrays for 2D cross-borehole electrical tomography surveys. Geophysical Prospecting, 62, p. 172–189.

Loke, M.H., Wilkinson, P.B., Uhlemann, S.S., Chambers, J.E. and Oxby, S., 2014b. Computation of optimized arrays for 3-D electrical imaging survey. Geophysical Journal International, 199, p. 1751–1764.

Militzer, H., Rösler, R. and Lösch, W., 1979. Theoretical and experimental investigations for cavity research with geoelectrical resistivity methods. Geophysical Prospecting, 27, p. 640–652.

Nimmer, R.E., Osiensky, J.L., Binley, A.M., Williams, B.C., 2008. Three-dimensional effects causing artifacts in twodimensional, cross-borehole, electrical imaging. Journal of Hydrology, 359, p. 59-70.

Nyquist, J. E., Peake, J. S., Roth M. J. S., 2007. Comparison of an optimized resistivity array with dipole-dipole soundings in karst terrain. Comparison of an optimized resistivity array with dipole-dipole soundings in karst terrain, 72(4), F139-F144.

Slater, L., Binley, A.M., Daily, W. and Johnson, R., 2000. Cross-hole electrical imaging of a controlled saline tracer Injection. Journal of Applied Geophysics 44, p. 85–102.

Stummer, P., Maurer, H., and Green, A.G., 2004. Experimental design: electrical resistivity data sets that provide optimum subsurface information. Geophysics, 69, n 1, pp.120–139.

Tsourlos, P., Ogilvy, R., Papazachos, C., Meldrum, P., 2011. Measurement and inversion schemes for single borehole-to-surface electrical resistivity tomography surveys. Journal of Geophysics and Engineering, vol. 8, n 4.

Wilkinson, P. B., Meldrum, P. I., Chambers, J. E., Kuras, O., and Ogilvy, R. D., 2006. Improved strategies for the automatic selection of optimized sets of electrical resistivity tomography measurement configurations. Geophysical Journal International, 167, p. 1119–1126.

Wilkinson, P. B., Chambers, J.E., Lelliott, M., Wealthall, G.P. and Ogilvy, R.D., 2008. Extreme sensitivity of crosshole electrical resistivity tomography measurements to geometric errors. Geophysical Journal International, 173(1), p. 49-62.

Wilkinson, P.B., Meldrum, P.I., Kuras, O., Chambers, J.E., Holyoake, S.J., Ogilvy, R.D., 2010. High-resolution Electrical Resistivity Tomography monitoring of a tracer test in a confined aquifer. Journal of Applied Geophysics 70, p. 268–276.

Wilkinson, P. B., Loke, M. H., Meldrum, P. I., Chambers, J. E., Kuras, O., Gunn, D. A. and Ogilvy, R.D., 2012. Practical aspects of applied optimized survey design for electrical resistivity tomography. Geophysical Journal International, 189, p. 428–440.

Yang F.W. and Ward S.H., 1985. Single-borehole and cross-borehole resistivity anomalies of thin ellipsoids and spheroids. Geophysics, vol. 50, n. 4, p. 637-655.

FIGURE CAPTIONS

Figure 1. Dynamic model and stages used to simulate different positions of a plume in a migration process. Small vertical black squares represent the electrode location into boreholes BH1, BH2 and BH3; black arrow and grey squares (named A, B and C) simulate the plume direction and position at stages A, B and C, respectively. Panel 1 (light grey colored) represents the cross-hole measurements acquired between BH1 and BH2, and panel 2 (dark grey colored), the cross-hole measurements acquired between BH2 and BH3.

Figure 2. Electrode distribution schemes for the CH dipole-dipole arrays (CH AM-BN and CH AB-MN) and the CH pole-tripole array with the MN dipole in the two boreholes (CH AMN-B/A-BMN). Capital letters and red/blue points designate the electrode name and their position into the boreholes (A and B represent the current electrodes and, M and N, the potential ones); AM: vertical distance between the current and the potential electrodes; MN: vertical distance between the potential electrodes.

Figure 3. Sensitivity patterns for the CH dipole-dipole (CH AM-BN and CH AB-MN) and the CH pole-tripole (CH AMN-B). The letters A and B represent the current electrodes and, M and N, the potential ones. In each configuration, sensitivity was normalized by its maximum value.

Figure 4. Anomaly detection value (AD) calculated for the CH dipole-dipole (AM-BN and AB-MN) and the CH pole-tripole arrays at the three stages (A, B and C) of the dynamic model using a resistivity contrast Rc=0.1. Maximum absolute relative resistivity variation (Y-axis) versus AM (X-axis) and MN (colored lines) distances. Dashed line indicates a 10% of resistivity change as guidance only.

Figure 5. In-panel/off-panel sensitivity value (IOS) calculated using the CH dipole-dipole (AM-BN and AB-MN) and the CH pole-tripole arrays for all the three stages (A, B and C) of the dynamic model and a resistivity contrast, Rc=0.1. Maximum absolute relative apparent resistivity difference (Y-axis) versus AM (X-axis) and MN (colored lines) distances. Dashed line indicates a 10% of resistivity difference as guidance only.

Figure 6. Anomaly detection value (AD) calculated for the CH dipole-dipole (AM-BN and AB-MN) and the CH pole-tripole arrays at the three stages (A, B and C) of the dynamic model using a resistivity contrast, Rc=10. Maximum absolute relative apparent resistivity variation (Y-axis) versus AM (X-axis) and MN (colored lines) distances using panel 1. Dashed line indicates a 10% of resistivity change as guidance only.

Figure 7. In-panel/off-panel sensitivity value (IOS) calculated using the CH dipole-dipole (AM-BN and AB-MN) and the CH pole-tripole arrays for all the three stages (A, B and C) of the dynamic model and a resistivity contrast, Rc=10. Maximum relative apparent resistivity variation (Y-axis) versus AM (X-axis) and MN (colored lines) distances using panel 1 and panel 2 responses. Dashed line indicates a 10% of resistivity difference as guidance only.

Figure 8. Inversion models obtained using (from top to bottom): the CH dipole-dipole AM-BN (5740 data), the CH pole-tripole (3080 data), the CH dipole-dipole AB-MN (3500 data), the complete mixed (CH pole-tripole and CH dipole-dipole AB-MN with 6580 data) and the organized (1036 data) datasets at the three stages (A, B and C) of the dynamic model. Resistivity contrast Rc=0.1. Root mean square (rms) =1.2%. Small vertical black squares represent the electrode location into boreholes (BH1, BH2 and BH3). Each inversion included panel 1 and panel 2 responses.

Figure 9. Inversion models obtained using (from top to bottom): the CH dipole-dipole AM-BN (5740 data), the CH pole-tripole (3080 data), the CH dipole-dipole AB-MN (3500 data), the complete mixed (CH pole-tripole and CH dipole-dipole AB-MN with 6580 data) and the organized (1036 data) datasets at the three stages (A, B and C) of the dynamic model using a resistivity contrast Rc=10. Root mean square (rms)=1.2%. Small vertical black squares represent the electrode location into boreholes (BH1 and BH2). Each inversion included panel 1 and panel 2 responses.

Figure 10. Geometric factor behavior obtained using the CH dipole-dipole arrays: A) CH AM-BN and B) CH AB-MN, with different AM and MN distances.